Appendix B

The detail explanation of event reconstruction

B.1 Hit-PMT selection for vertex reconstruction

(1) The hit channels in 200nsec timing window containing the maximum number of hits are selected. The reason we use 200nsec at first is that the maximum time of flight for a direct photon is approximately that.

(2) The number of background hits in 200nsec window is estimated as follow;

$$N_{bg} = (t_3 - t_2) \times \frac{N_{hit}(t_1 : t_2) + N_{hit}(t_3 : t_4)}{(t_2 - t_1) + (t_4 - t_3)},$$

where $N_{hit}(t_i : t_j)$ is number of hit-PMT in the timing between t_i and t_j, and t is as shown in Fig B.1, t_1 and t_4 are the beginning and end of the event, and t_2 and t_3 are the limits of the time window under consideration.

(3) The maximum number of hits for each of 11 timing windows of width $(200 \times n/11, n = 11, 10, \ldots, 1)$ inside the 200nsec window determined above is calculated. For each window, the *significance* defined below is also calculated:

$$(significance) = \frac{N_{hit} - N_{bg}}{\sqrt{N_{bg}}}.$$

(4) The window with maximum significance is selected.

(5) It is checked whether any wider timing window than (4) with

$$(significance) > (significance)_{max} \times 0.8$$

exist or not. If one does exist, all hit channels in this wider window are used for vertex reconstruction are used. If not the timing window which has maximum significance is taken. This is so that we can use as many signal hits as possible.

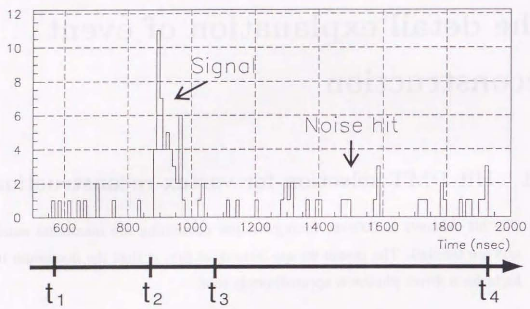

Figure B.1: The timing distribution of hit-PMTs in one event. The time, which is horizontal axis, is the relative timing of each hit-PMT obtained from ATM data.

B.2 The definition of effective N_{hit}

. The definition of effective N_{hit} (N_{eff}) is as the following equation,

$$N_{eff} = \sum_{i=1}^{N_{hit}} \left[(X_i + \epsilon_{tail} - \epsilon_{dark}) \times \frac{N_{all}}{N_{normal}} \times \frac{R_{\mathrm{cover}}}{S(\theta_i, \phi_i)} \times \exp\left(\frac{r_i}{\lambda(\mathrm{run})}\right) \times G_{time}(i) \right] \quad \text{(B.1)}$$

The first factor is the correction to the each hit, where X_i is "occupancy" in order to estimate the effect of multi photo-electrons, ϵ_{tail} is for the correction for late hits outside

the 50ns window, and ϵ_{dark} is for dark noise correction. The definition of X_i is as follows:

$$X_i = \begin{cases} \dfrac{\lambda_i}{x_i} = \dfrac{\log \frac{1}{1-x_i}}{x_i} & x_i < 1 \\ 3 & x_i = 1 \end{cases} \quad \text{(B.2)}$$

where x_i is the ratio of number of hit-PMTs to the number of PMTs around the i-th hit-PMT (normally nine (3×3)) and λ_i is the estimated number of photons per one PMT in this 3×3 PMTs region. This correction is to estimate the number of photons arrived at the i-th hit-PMT using the number of PMTs which does not hit in the 3×3 PMTs region around the i-th hit-PMT. Here, the ratio of the PMTs which does not hit is measured to be $1 - x_i$. As while, when λ_i is the average number of photons per one PMT in the 3×3 PMTs region, the probability not to hit is calculated by Poisson distribution as shown in the following equation,

$$P_0 = \frac{(\lambda_i)^0 \times e^{-\lambda_i}}{0!} = 1 - x_i. \quad \text{(B.3)}$$

Fig B.2 shows the occupancy as a function of the number of hit-PMTs around one hit-PMT. When $x_i = 1$, the occupancy diverge, therefore, we determined that $X_i = 3$ at $x_i = 1$ by extrapolation as is seen in Fig B.2. It also minimizes the position dependence of N_{eff}

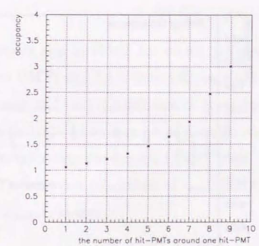

Figure B.2: The occupancy as a function of the number of hit-PMTs around one hit-PMT.

The second factor is the bad PMT correction, where N_{all} is the total number of PMTs, 11146, and N_{normal} is the number of properly operating PMTs for the relevant subrun.

The third factor is the effective photo coverage. The average of the photo coverage, which is the ratio of the area covered by PMT to all area, is 0.4041, (R_{cover}). However, the effective photo coverage changes as the input angle of the photon to the PMT.

Therefore, we applied the coverage correction, where $S(\theta_i, \phi_i)$ is the photo coverage from a view of θ_i, ϕ_i direction.

The fourth factor is the water transparency correction, where r_i is the distance from the reconstructed vertex to the i-th hit-PMT position, λ is water transparency as shown in Fig 4.12.

The fifth factor, $G_{time}(i)$, is the gain correction at single photo-electron level which depends on the time of the production of each PMT.

B.3 Recent results of LINAC calibration

We recently took calibration data using an electron LINAC. This data taking was performed at 6 pipe positions and 7 beam energy points. The positions are $(x, z) =$ $(-4, 0)$, $(-4, 12)$, $(-8, 0)$, $(-8, 12)$, $(-12, 0)$ and $(-12, 12)$ (m), all at $y = -0.7$m and the beam energies are shown in Table 5.2. Fig B.3 shows the difference of energy scale between data and Monte Carlo. The position dependence of the difference is less than 1% and the energy dependence is less than 0.3%. The differences of the energy, position and directional resolution between data and Monte Carlo are summarized in Table B.1.

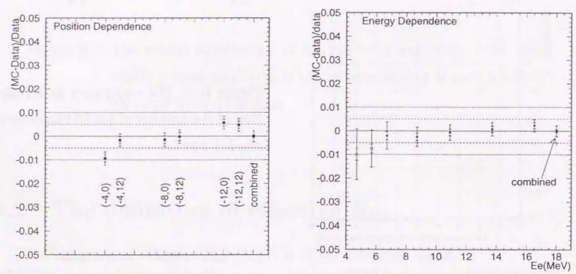

Figure B.3: The difference of energy scale between data and Monte Carlo. The left figure shows the position dependence and the right one shows the energy dependence

Energy resolution	$< 2\%$
Position resolution	$< \pm 5cm$
Directional resolution	1.8 degree at 6.5MeV
	0.3 degree at 16MeV

Table B.1: The differences of the energy resolution ((data-MC)/data), the position resolution (data-MC) and the directional resolution (data-MC) between data and Monte Carlo in new LINAC calibration data.

B.4 Another algorithm of vertex reconstruction

As described in Section 7.2, we use a different algorithm of vertex reconstruction in order to reject the type of noise event shown in Fig 7.8. The essence of this reconstruction is selecting PMT hits which are considered to be caused by Cherenkov photons. For this purpose, we use the space-time correlation of hit-PMTs. The following criteria is applied in selecting PMTs: if a hit-PMT doesn't have neighboring hit-PMTs which satisfy the following condition,

$$\Delta r \leq r_{limit} \quad \text{and} \quad \Delta t \leq t_{limit},$$

we reject this hit-PMT for vertex reconstruction, where Δr is the spatial distance between PMTs and Δt is time difference between these PMTs. r_{limit} and t_{limit} are limits of distance and timing difference of given PMTs. These limits are chosen so that they reduce the dark noise as much as possible without reducing good PMT significantly. These limits are determined using LINAC data. Table B.2 shows the number of remained hit-PMTs in several conditions of r_{limit} and t_{limit}. For this analysis we take $r_{limit} = 700cm$ and $t_{limit} = 35nsec$.

Fig B.4 shows the distribution of the distance (Δl) between the original vertex and the vertex from the new method. Some typical events with large Δl are shown in Fig 7.8. The vertex reconstruction of events with large Δl is generally clearly mistaken. Therefore, we use Δl for the event reduction as follows; events with $\Delta l > 5m$ are rejected. The rejected events are classified by the number of small clusters as follows: $\sim$24% have two

r_{limit} (cm)	t_{limit} (nsec)	Number of hit-PMTs	Ratio (%)
400	20	40406	50
500	25	47907	60
600	30	53756	67
700	35	59054	74
800	40	63781	79

Table B.2: The number of remained hit-PMTs in several conditions to be neighboring PMTs, and r_{limit} and t_{limit} are given in the text. The number of all hit-PMTs is 80236. This is 5MeV LINAC data.

clusters;~57% have one cluster; and ~19% have none.

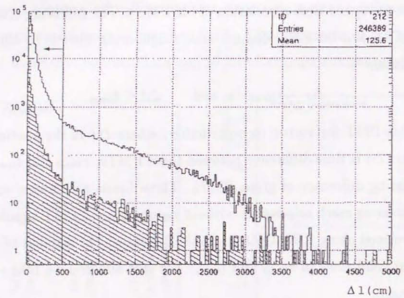

Figure B.4: The distribution of the distance between the original vertex and the vertex from the new method. These are the ^{8}B Monte Carlo and the data after spallation cut (hatched region).

B.5 The method of event clean up using vertex and direction

In addition to the criteria described above, we use the uniformity of the azimuthal angle distribution of hit-PMTs for identification of the event as shown in Fig 7.8.

The frame of reference has its center of the reconstructed vertex and the pole is the event direction. From this, the azimuth angle is calculated. Fig B.5 shows typical normal and noise events, and the azimuth angle distributions of each. The expected distribution is the dashed line, and we use the length of the arrow shown in the figure for the identification. If the event is normal, the hit-PMT distribution is uniform and the value is small, but if there is a cluster, the value is large.

Fig B.6 shows the scatter plot of this value and the difference between fitted and generated vertex in solar neutrino Monte Carlo events. This shows only mis-reconstructed events have large values.

Fig B.7 shows the distribution of the azimuthal angle non-uniformity in the final sample and in the solar neutrino Monte Carlo in two energy regions. The cut criteria is 0.4, and the efficiency is shown in the figure.

Fig B.8 shows the efficiency of the complete reduction combined with both methods described in Section B.4 and B.5 in real data and Monte Carlo. From the figure, we can see the real data and Monte Carlo are very consistent above our analysis threshold energy; the maximum of difference is 0.7%. This is taken as a systematic error in the solar neutrino analysis.

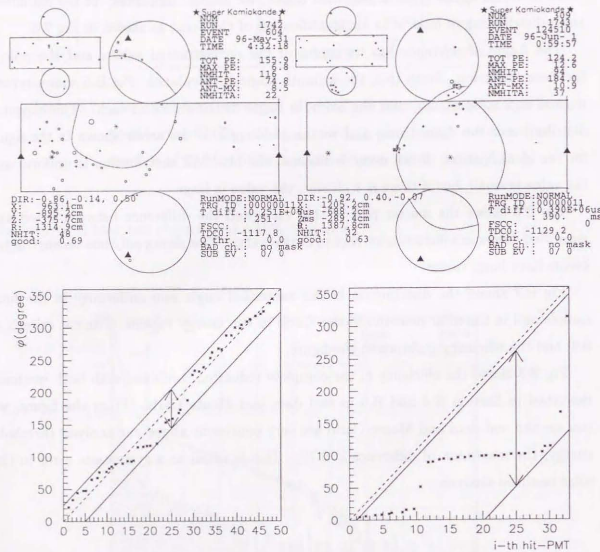

Figure B.5: The left figure is shown as normal event and the right one is the event with small cluster. Lower distribution fill the azimuth angle of each hit-PMT from the start of one point.

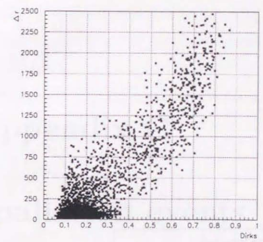

Figure B.6: The relation of the uniformity of the azimuth angle distribution and the difference between fitted and generated vertex in Monte Carlo. The horizontal axis is normalized to 1.

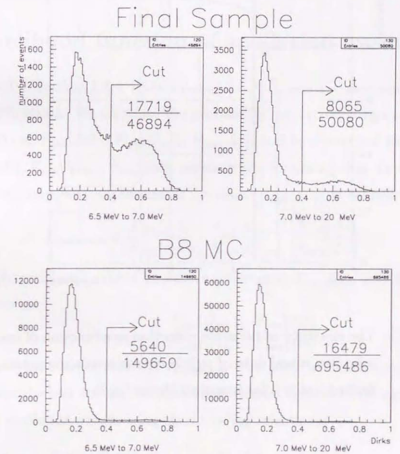

Figure B.7: The distribution of the azimuthal angle non-uniformity in the final sample and in the solar neutrino Monte Carlo in two energy regions. The numbers in the figure show the number of cut event and all event.

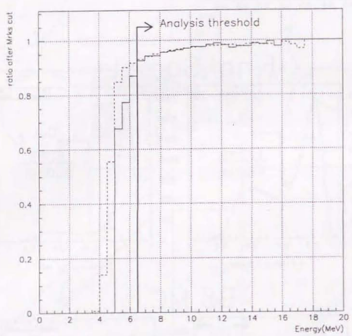

Figure B.8: The efficiency of the noise reduction as a function of energy. The solid line is real data of tightly chosen spallation events, and the dashed line is solar neutrino Monte Carlo.

Appendix C

Spallation events

C.1 Likelihood function of spallation event

As described in Section 7.2.4, three values ($\triangle L$, Q_{res} and $\triangle t$) are used for the spallation likelihood function. We calculate the probability density functions of $\triangle L$, Q_{res} and $\triangle t$ by spallation as $F_{spa}(\triangle L)$, $F_{spa}(Q_{res})$, $F_{spa}(\triangle t)$, and by events not caused by spallation as $F_{non}(\triangle L)$, $F_{non}(Q_{res})$, $F_{non}(\triangle t)$, respectively. Assuming that above three factors are independent, the spallation likelihood function ($L_{spallation}$) is defined as follows,

$$L_{spallation} \equiv \frac{F_{spa}(\triangle L)}{F_{non}(\triangle L)} \cdot \frac{F_{spa}(Q_{res})}{F_{non}(Q_{res})} \cdot \frac{F_{spa}(\triangle t)}{F_{non}(\triangle t)} \tag{C.1}$$

For muons with tracks that cannot be well reconstructed, $L_{spallation}$ is defined using only two parameters:

$$L_{spallation} \equiv \frac{F_{spa}(Q_{res})}{F_{non}(Q_{res})} \cdot \frac{F_{spa}(\triangle t)}{F_{non}(\triangle t)} \tag{C.2}$$

Spallation events have larger values of $L_{spallation}$ than solar neutrino events.

Here, we describe how to find the probability density function. We gather samples of predominantly spallation events using the following selections,

- $\triangle t \leq 0.1 sec.$ and $N_{eff} \geq 50$ for $\triangle L$
- $\triangle t \leq 0.1 sec.$ and $N_{eff} \geq 50$ for Q_{res}
- $Q_{res} \leq 5.0 \times 10^5 p.e.$ and $\triangle L \leq 3m$ for $\triangle t$

where we cut on N_{eff} because very low energy events are often caused by other background sources.

The distribution of $\triangle L$ is made in six Q_{res} ranges as shown in Fig 7.11. In each histogram, the spallation component and phase space shown by dashed line ($F_{non}(\triangle L)$) are included. Subtracting this phase space from the distribution, we get $F_{spa}(\triangle L)$.

The likelihood function for Q_{res} is defined the same way as for $\triangle L$. Fig C.1 shows the Q_{res} distribution of muons accompanied with a spallation event (a), and of muons without an associate spallation candidates (b). Subtracting (b) from (a), we can get the Q_{res} distribution from only the spallation component (c) ($F_{spa}(Q_{res})$).

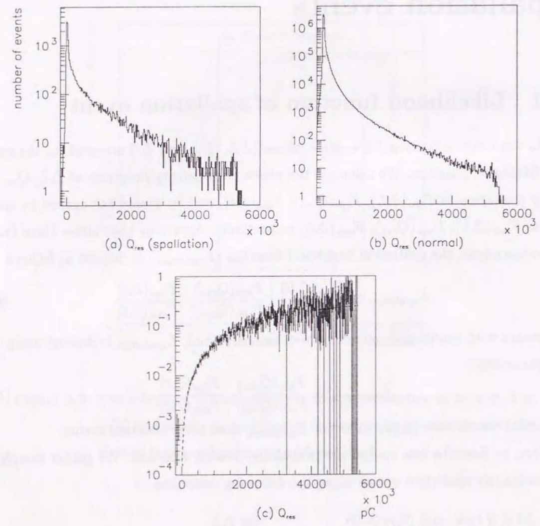

Figure C.1: The Q_{res} distribution of muons accompanied with a spallation event (a), of muons without any associated spallation candidates (b), and from only the spallation component (c), which is the differences (b) and (a).

Fig C.2 shows ($\triangle t$) distribution. One can see a decay curve in correlation with the penetrating muons. This decay curve is the combination of many isotopes with different half-lifes as shown in Table 7.1. For making the likelihood function for $\triangle t$, the decay curve as shown in Fig C.2 is fitted with the combination of isotopes with known half-life. The result is:

$$\begin{aligned}\frac{F_{spa}(\triangle t)}{F_{non}(\triangle t)} &= 33900 \times 2^{-\frac{\triangle t}{0.011}} + 120100 \times 2^{-\frac{\triangle t}{0.0204}} + 338.6 \times 2^{-\frac{\triangle t}{0.178}} + 1254 \times 2^{-\frac{\triangle t}{0.84}} \\ &+ 134.7 \times 2^{-\frac{\triangle t}{2.449}} + 676.1 \times 2^{-\frac{\triangle t}{7.134}} + 7.791 \times 2^{-\frac{\triangle t}{13.8}} \qquad \text{(C.3)}\end{aligned}$$

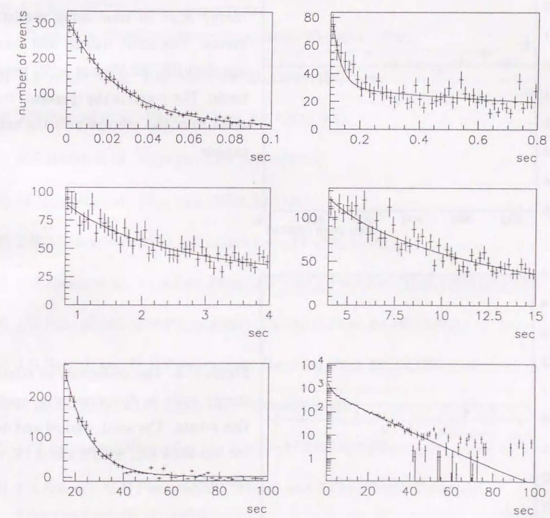

Figure C.2: The $\triangle t$ distribution in several time range. The solid lines show fitting results.

C.2 Spallation events as detector calibration

Spallation events are generated uniformly in volume, in direction and in time. Therefore, we can use these events as a good relative calibration source. Fig C.3 and Fig C.4 show the stability of relative energy scale in time and as a function of nadir, respectively. The uniformity of energy scale both in time and in direction are stable less than ±0.5%.

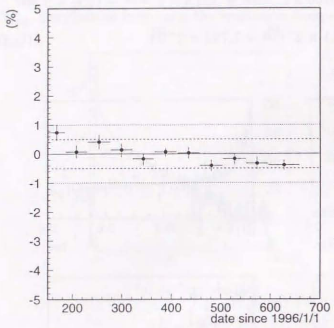

Figure C.3: The stability of relative energy scale in time using spallation events. The solid, dashed and dotted line show 0%, ±0.5% and ±1%, respectively. The y-axis is the (percent) deviation from the average over the entire sample.

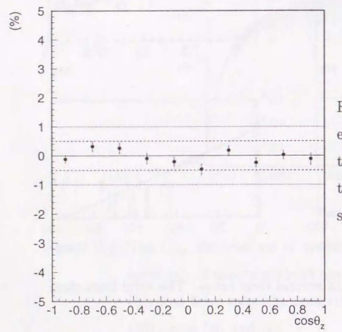

Figure C.4: The uniformity of relative energy scale in direction using spallation events. The solid, dashed and dotted line show 0%, ±0.5% and ±1%, respectively.

Bibliography

[1] H.A.Bethe, Phys.Rev.,**55**,434(1939).

[2] J.N.Bahcall, "*Neutrino Astrophysics*" (Cambridge University Press, Cambridge, England, 1989).

[3] R.Davis,Jr. et al., Phys.Rev.Lett.,**20**,1205(1968).

[4] J.N.Bahcall et al., Phys.Rev.Lett.,**20**,1209(1968).

[5] K.S.Hirata et al., Phys.Rev.Lett.,**63**,16(1989).

[6] W.Hampel et al., Phys.Lett.**B388**,384(1996).

[7] J.N.Abdurashitov et al., Phys.Rev.Lett.,**77**,4708(1996).

[8] K.S.Hirata et al., Phys.Rev.,**D44**,2241(1991); Phys.Rev.,**D45**,2270(1992)(E).

[9] J.N.Bahcall and M.H.Pinsonneault, Rev.Mod.Phys.,**64**,885(1992).

[10] J.N.Bahcall and M.H.Pinsonneault, Rev.Mod.Phys.,**67**,78(1995).

[11] S.Turck-Chièze and I.Lopes, Ap.J.**408**,347(1993).

[12] J.Christensen-Dalsgaard et al., Science,**272**,1286(1996).

[13] J.N.Bahcall, M.H.Pinsonneault, S.Basu and J.Christensen-Dalsgaard, Phys.Rev.Lett.,**78**,171(1997).

[14] C.W.Johnson et al., Astrophys.J.,**392**,320(1992); M.Kamionkowski and J.N.Bahcall, Phys.Rev.,**C49**,545(1994).

[15] T.Motobayashi et al., Phys.Rev.Lett.,**73**,2680(1994).

[16] A.Dar and G.Shaviv, Technion report,(1994); astro-ph/9401043.

[17] J.N.Bacall et al., astro-ph/9404002; A.Dar and G.Shaviv, astro-ph/9404035.

[18] K.lande and P.S.Wildenhain, "*Proceeding of the 17th international conference on neutrino physics and astrophysics*" (1996), (World Scientific, 1997), p25.

[19] R.Davis, Prog.Part.Nucl.Phys.,**32**,13(1994).

[20] Y.Fukuda et al., Phys.Rev.Lett.,**77**,1683(1996).

[21] M.Cribier, talk at "*Fifth international workshop on Topics in Astroparticle and Underground Physics*" (1997).

[22] N.Hata and P.Langacker, IASSNS-AST 97/29, UPR-751T(1997).

[23] B.Pontecorvo, Sov.Phys.JETP,**6**,429(1957);
Z.Maki, M.Nakagawa, and S.Sakata, Prog.Theor.Phys.**28**,870(1962).

[24] J.N.Bahcall and S.C.Frautschi, Phys.Lett.**B29**,263(1969).

[25] S.L.Glashow and L.M.Krauss, Phys.Lett.**B190**,199(1988).

[26] P.I.Krastev and S.T.Petcov, Phys.Rev.,**D53**,1665(1996).

[27] L.Wolfenstein, Phys.Rev.,**D17**,2369(1978); **D20**,2634(1979).

[28] S.P.Mikheyev and A.Yu.Smirnov, Yad.Fiz.**42**,1441(1985).

[29] S.J.Parke, Phys.Rev.Lett.,**57**,1275(1986).

[30] T.K.Kuo and J.Pantaleone, Rev.Mod.Phys.,**61**,937(1989).

[31] D.L.Anderson, "*Theory of the Earth*"
(Blackwell scientific publications, 1989).

[32] I.Frank and I.Tamm, C.R.Acad.Sci.USSR,**14**,109(1937).

[33] E.D.Commins and P.H.Bucksbaum, "*Weak interactions of Leptons and Photons*", (Cambridge University Press, Cambridge, England, 1983).

[34] J.N.Bahcall et al., Phys.Rev.,**D51**,6146(1995).

[35] H.Kume et al., Nucl.Instr.and Meth.,**205**,299(1983).

[36] A.Suzuki et al., Nucl.Instr.and Meth.,**A329**,299(1993).

[37] T.Tanimori, H.Ikeda, M.Mori, K.Kihara, H.Kitagawa, and Y.Haren,
IEEE Trans.Nucl.Sci.,**NS-36**,497(1989).

[38] Y.Kitaguchi, master thesis (1997) (unpublished).

[39] E.Ichihara, master thesis (1996) (unpublished).

[40] N.Sakurai, master thesis (1998) (unpublished).

[41] G.A.Bartholomew, et al., Nucl.Data,**A3**,367(1967).

[42] A.F.M.Ishaq, et al., Z.Physik,**A281**,365(1977).

[43] T.Maruyama, master thesis (1996) (unpublished).

[44] F.Halzen and A.D.Martin, "*Quarks and Leptons, An Introductory Course in Modern Particle physics*", (John Wiley & Sons, Inc., New York, 1984).

[45] "GEANT - Detector Description and Simulation Tool", CERN Program Library (1993).

[46] Y.Koshio, master thesis (1994) (unpublished).

[47] J.Phys.Chem,Ref.Data, vol.14 No.4 (1985).

[48] A.Morel et al., Limnology and Oceanography 22(1977)709.

[49] H.A.Maclead, Thin-Film Optical Filters, (1986),
and private communication with Hatakeyama.

[50] R.Serber, Phys.Rev.,**72**,1114(1947).

[51] G.Rudstam, Phil.Mag.,**46**,344(1955); J.J.Griffin, Phys.Rev.Lett.,**17**,478(1966); Feshback, Koonin and Kerman, Ann.Phys.,**125**,329(1980).

[52] M.Nemoto, master thesis (1998) (unpublished).

[53] A.Cumming and W.C.Haxton, Phys.Rev.Lett.,**77**,4286(1996).

[54] B.Ricci et al., astro-ph/9705164.

[55] Q.Y.Liu, M.Maris, and S.T.Petcov, hep-ph/9702361; M.Maris, and S.T.Petcov, hep-ph/9705392.

[56] KEK Data Acquisition Development Working Group, "TKO Specification",KEK Report 85-10,(1985)

84

スーパー神岡実験における太陽ニュートリノの研究